NJC

ROYAL SOCIETY OF CHEMISTRY

PAPER

View Article Online
View Journal

Cite this: DOI: 10.1039/d5nj01928a

Anchoring metal cobalt species on defective alumina for enhanced catalytic performance in FT synthesis

Qiuyao Jiao,[a] Yan Liu,*[b] Ran Yu[a] and Lei Li*[a]

In metal-supported heterogeneous catalysts, the metal–support interaction (MSI) is a very important factor for determining the catalytic performance. Herein, commercial γ-alumina was reduced with hydrogen in advance, providing strong anchoring sites for the metal (metal oxide) species. This research demonstrated the use of pre-reduced alumina as a catalyst carrier over the unreduced one for anchoring metal Co species during the FTS. The defective-alumina-supported catalyst displayed superior performance. The Co/RAl$_2$O$_3$-550 catalyst showed a surprisingly high CO conversion rate of 56.0%, C_{5+} hydrocarbon selectivity rate of 93.2%, and a low methane selectivity of 2.7% while exhibiting a remarkably high activity (CTY = 1.1 × 10^{-5} molCO g_{Co}^{-1} s^{-1}). It was revealed that the strong reduction of alumina generated more defective sites, which strongly anchored metal cobalt species onto it *via* MSI. Besides, the reduction of alumina also boosted the number of surface L-acid sites, promoting the CO absorption rate through CO dissociation. These results reveal the unique properties of defective-Al_2O_3-supported cobalt catalysts and provide a practical strategy to explore stable and efficient FTS catalysts.

Received 7th May 2025,
Accepted 21st July 2025

DOI: 10.1039/d5nj01928a

rsc.li/njc

Introduction

Due to the increasing environmental and energy issues, the Fischer–Tropsch synthesis (FTS) is receiving wide research interest as an important gas-to-liquid (GTL) process, in which synthesis gas (CO + H_2) is used to produce high-quality ultra-clean fuels and high-value chemicals.[1,2] It is well-known that cobalt-based catalysts preferentially contribute to high activity and high selectivity towards long chain n-paraffins. Therefore, it is necessary to develop Co-based catalysts for synthesizing liquid fuels.

For employing Co-based catalysts in the FTS, more efforts have been devoted to prepare different catalysts with improved metal dispersion and exposed metallic cobalt atoms, resulting in improved catalytic activity and increased selectivity toward the desired long-chain hydrocarbons.[3–8] Besides, metal–support interaction (MSI), which strongly affects a catalyst's electronic structure, geometric structure and chemical composition, is considered an essential factor that determines its catalytic performance.[9,10] Qin *et al.*[11] fabricated a stable Co@C-SiO_2 catalyst using silica and intermediate carbon as a protective shell. The moderate MSI endowed by carbon and the confined structure maintained a single-crystal structure, leading to its long-term stable performance with a low CH_4 selectivity and high CO conversion and C_{5+} selectivity. Wang *et al.*[12] prepared cobalt catalysts loaded on SiO_2-modified Al_2O_3@Al composites. They found that the decreased MSI *via* the modification of SiO_2 raised the CO activity and C_{5+} selectivity and decreased the CH_4 selectivity. Moreover, Al_2O_3-modified TiO_2 improved the Co dispersion, whereas SiO_2-modified TiO_2 boosted the reducibility of Co species, both of which could improve the activity per gram of Co.[13] Similarly, hydrothermal carbon-coated TiO_2 support facilitated the dispersion and reducibility of cobalt species, contributing to enhanced activity and stability during the FTS.[14] Therefore, the regulation of metal–support interaction is considered an effective strategy for optimizing FTS performance.

It is well accepted that Al_2O_3-supported cobalt catalysts have attracted wide research attention in the FTS in the past decade. As classic FTS catalyst supports, different alumina phases have been studied at a constant Co particle size, and their C_{5+} selectivity followed the order of Co/α-Al_2O_3 > Co/δ-Al_2O_3 > Co/θ-Al_2O_3 > Co/γ-Al_2O_3.[15] The prepared catalysts with medium pore sizes showed a higher C_{5+} selectivity than the catalysts with small pore sizes.[16] C_{5+} selectivity is also related to both the particle size and support.[17] Recently, a defective alumina with

[a] School of Chemistry and Chemical Engineering, Yancheng Institute of Technology, Yancheng, 224051, P. R. China. E-mail: lee_ycit@hotmail.com
[b] State Key Laboratory of Coal Conversion, Institute of Coal Chemistry, Chinese Academy of Sciences, Taiyuan 030001, Shanxi, P. R. China. E-mail: liuyan@sxicc.ac.cn

rich penta-coordinated Al^{3+} sites was developed as a catalyst support with superior catalytic activity. Kwak *et al.*[18] reported the activation of γ-alumina by pre-reduction with hydrogen, yielding more coordinatively unsaturated Al_{penta}^{3+} sites, which could be strong anchoring sites for metal (or metal oxide) species. Using a similar catalyst design concept, nanoceria particles were anchored on Al_{penta}^{3+} sites of activated γ-alumina, forming noble metal (Pt, Pd and Rh)-ensembled catalysts with 100% dispersion.[19] Huang *et al.*[20] successfully fabricated efficient and stable Al_2O_3/Pd/SiO_2 catalysts by the atomic layer deposition (ALD) method, revealing that the abundant penta-coordinated Al^{3+} sites could interact strongly with the adjacent surface PdO_x phases to form stable PdO_x and Pd^0-PdO_x structures, resulting in excellent activity for methane combustion reaction. The rich unsaturated, pentacoordinated Al^{3+} sites could promote the dispersion of metal active species and stabilize the electronic valence state of the metal, strengthening the metal–support interaction.[21,22] Based on this strategy, the special MSI and metal Co dispersion in defective-γ-alumina need to be explored further for understanding their unique structure-performance relationship in the FTS.

Herein, commercial alumina (γ-Al_2O_3) was pre-reduced using hydrogen, in which the number of Al_{penta}^{3+} sites increased with the increasing treatment temperature. The resultant alumina was applied to the construction of Co-based FTS catalysts. The properties of the carrier, metal dispersion and metal–support interaction were deeply explored based on varied characterizations. Compared with the unreduced Al_2O_3-supported catalyst, the serial Co/RAl_2O_3-*T* catalysts showed improved CO conversion and C_{5+} selectivity and low CH_4 selectivity.

Experimental

Catalyst preparation

The typical procedure to synthesize Co/RAl_2O_3 catalyst samples was as follows: the commercial γ-alumina (AR, Aladdin Chemistry Co., Ltd.) was activated by reduction under a 10% H_2:N_2 flow at different temperatures (*e.g.*, 350, 450 and 550 °C) for 1 h to yield coordinatively unsaturated Al_{penta}^{3+} sites (named as RAl_2O_3-*T*).[18] Subsequently, the 20 wt% Co/RAl_2O_3-*T* catalyst was prepared *via* an impregnation method. In contrast, unreduced γ-Al_2O_3-supported Co catalyst was also prepared. The detailed preparation process is provided in the SI.

Characterizations

The different Co-based catalysts were characterized by XRD, BET, TEM, XPS, H_2-TPR/TPD, Al-NMR, CO-TPD, CO-TPSR and *in situ* FTIR techniques. The detailed methods are described in the SM.

Catalytic performance

The performance of these catalysts during FTS was evaluated on a stainless-steel fixed-bed reactor. The detailed operations are described in the SM.

Results and discussion

The defective-Al_2O_3-supported Co catalyst (Co/RAl_2O_3) was prepared by an impregnation method employing reduced Al_2O_3 as supports (Fig. 1). As a most commonly used catalyst support material, γ-Al_2O_3 is used to support active metal phase with high dispersion and thermal stability. Koningsberger and co-workers[23] suggested that specific interactions between "defect sites" of γ-Al_2O_3 and Pt clusters play an essential role, converting 3D Pt particles into 2D rafts during the annealing process. Due to these defect sites, the presence of monoatomically dispersed Pt on γ-Al_2O_3 was confirmed using high-angle annular dark-field scanning transmission electron microscopy.[24] Szanyi *et al.*[18] used coordinatively unsaturated Al^{3+} centers [*i.e.*, pentacoordinated Al^{3+} (Al_{penta}^{3+})] on γ-Al_2O_3 surface] for anchoring the Pt species. Inspired from these outstanding works, herein, the defective-γ-Al_2O_3, pre-reduced under 10% H_2/N_2 atmosphere at different temperatures (*e.g.*, 350, 450 and 550 °C), was employed as support for anchoring cobalt oxide. The cobalt oxide strongly interacted with defective-γ-Al_2O_3 and was further reduced to metal Co active phase before the FTS reaction.

Fig. 2A shows the XRD patterns of different catalysts. Except for the diffraction peaks of Co_3O_4 (JCPDS#: 42-1467), one diffraction peak at *ca.* 67.0° was assigned to the characteristic peak of γ-Al_2O_3 (JCPDS#: 10-0425).[25] Notably, the reduction process did not change the bulk crystalline phase of γ-Al_2O_3. Furthermore, the average crystallite sizes of Co_3O_4 were calculated using the Scherrer equation based on the (311) plane. The particle sizes were 12.90, 12.52, 12.73 and 13.49 nm for the Co/Al_2O_3, Co/RAl_2O_3-350, Co/RAl_2O_3-450 and Co/RAl_2O_3-550 samples, and the corresponding Co particle sizes were estimated to be 9.7, 9.4, 9.5 and 10.1 nm, respectively (Table 1). These finding indicated that the average metal Co particle size changed slightly over reduced and unreduced Al_2O_3 support. In addition, this slight difference might be related with the change in the surface microstructure of Al_2O_3 treated with hydrogen at different temperatures.

The interaction of Al^{3+} sites with cobalt was investigated by the ^{27}Al solid-state MAS-NMR spectra. As shown in Fig. 2B, the characteristic signals centered at around 10, 35, and 67 ppm chemical shift could be attributed to Al^{3+} species,

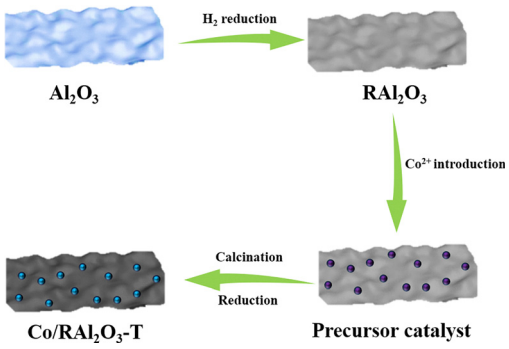

Fig. 1 Schematic of the preparation of Co/RAl_2O_3 catalysts.

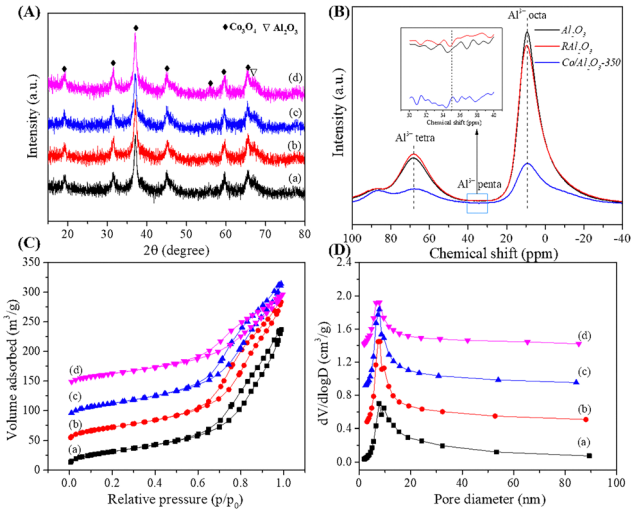

Fig. 2 (A) XRD profiles of different Co/Al_2O_3 samples, (B) ^{27}Al NMR spectra of fresh Co/Al_2O_3 samples, and the localized spectra between 30 and 40 ppm (inset), (C) N_2 adsorption–desorption isotherms, and (D) pore size distribution. (a) Co/Al_2O_3, (b) Co/RAl_2O_3-350, (c) Co/RAl_2O_3-450, (d) Co/RAl_2O_3-550.

corresponding to the octahedral (Al^{3+}_{octa}), pentahedral (Al_{penta}^{3+}), and tetrahedral (Al^{3+}_{tetra}) coordination environments, respectively.[19,20,27] By comparing the unreduced and reduced Al_2O_3, we found that the intensity of Al^{3+}_{octa} peak decreased and the intensity of Al^{3+}_{tetra} peak increased, and basically no Al_{penta}^{3+} peak was observed. Once the Co species were introduced into the surface of reduced Al_2O_3, both the intensities of Al^{3+}_{octa} and Al^{3+}_{tetra} peaks clearly decreased. Unfortunately, there was no significant change for the characteristic signal of Al_{penta}^{3+} in all the samples (the inset of Fig. 2B). Nevertheless, in view of the characterization of surface acid property, the unsaturated Al_{penta}^{3+} sites could have formed on γ-Al_2O_3 surface for anchoring the supported metal particles due to the dehydration and dihydroxylation processes.[18,28] This finding suggested that the Al_{penta}^{3+} sites disappeared after loading of the cobalt species, and the cobalt species would be preferentially occupying the Al_{penta}^{3+} sites through the formation of Co–O–Al, followed by the Al^{3+}_{octa} or Al^{3+}_{tetra} sites.

N_2 sorption analysis was employed to characterize the specific surface area and pore structure of different catalysts (Fig. 2C and D). All the samples exhibited type-IV sorption isotherm with hysteresis loops at high relative pressure ($P/P_0 > 0.7$), implying the existence of mesopores due to the stacked holes. Unlike the other three samples, the hysteresis loop of Co/RAl_2O_3-550 sample changed slightly, which might be the result of strong reduction. The surface area, pore volume and pore size of all the samples are summarized in Table 1. It can be seen that the surface areas of Co/Al_2O_3, Co/RAl_2O_3-350 and Co/RAl_2O_3-450 are kept at *ca.* 140 $m^2\ g^{-1}$, but the surface area of Co/RAl_2O_3-550 decreased to *ca.* 126 $m^2\ g^{-1}$. Similarly, compared with the other three samples, the pore volume and pore size of Co/RAl_2O_3-550 decreased accordingly. It was reported that the H_2 reduction of fresh γ-alumina were centered at 267 and 661 °C in TPR study, attributed to the reduction of weakly coordinated surface aluminum and the reduction of strongly coordinated bulk aluminum, respectively.[19,26] Thus, it is reasonable to assume that the surface microstructure of Al_2O_3 changed when it was treated with hydrogen at high temperature (*e.g.*, 550 °C). This change could affect the dispersion of cobalt species on the surface of Al_2O_3, resulting in an obvious decrease in the surface area and pore volume.

Fig. 3 shows the TEM images of different catalysts. The distributions of cobalt oxides on the different Al_2O_3 supports are clearly observed. It can be seen that all catalysts exhibited different states of aggregation, and the particle size of cobalt oxides ranged from a few nanometres to several tens of nanometres. In contrast, the commercial Al_2O_3-supported catalyst (Co/Al_2O_3) exhibited an obvious aggregation of cobalt oxide with large particle size. Based on the XRD analyses, there is no obvious change in the particle size of cobalt supported on reduced or unreduced Al_2O_3. Previous studies indicated that the rich unsaturated, pentacoordinated Al^{3+} sites on Al_2O_3 could promote the dispersion of metal active species.[21,22] Due to the aggregation state, cobalt dispersion cannot be distinguished in the TEM images. Thus, in order to explore cobalt dispersion, an H_2-TPD measurement was necessary.

XPS was performed to study the surface composition and chemical state of different catalysts, and the fitted results are displayed in Fig. 4 and Table S1. As shown in Fig. 4, the typical Co $2p_{3/2}$ and Co $2p_{1/2}$ peaks were found at *ca.* 780.2 and 795.5 eV, respectively, with a peak distance of *ca.* 15 eV, demonstrating the presence of Co_3O_4 phase.[29] The Co $2p_{3/2}$ peak was deconvoluted into three components, corresponding to Co^{3+} (*ca.* 779.9 eV), Co^{2+} (*ca.* 782.0 eV), and the shake-up satellites (*ca.* 786.7 eV), respectively.[6,30] As shown in Table S1, the surface Co/Al ratios in different catalysts followed the order, of Co/RAl_2O_3-350 < Co/Al_2O_3 < Co/RAl_2O_3-450 < Co/RAl_2O_3-550. This trend indicated that the reduction of Al_2O_3 support can improve the concentration of surface cobalt species. In

Table 1 Physicochemical properties of different Co/Al_2O_3 catalysts

Sample	Co contents[a] (wt%)	S_{BET} ($m^2\ g^{-1}$)	Pore volume ($m^3\ g^{-1}$)	Pore size (nm)	d(Co)[b] (nm)	Dispersion (%)[c]	H_2 desorbed (μmol g^{-1})[c]
Co/Al_2O_3	17.58	143.2	0.38	10.6	9.7	11.5	291.7
Co/RAl_2O_3-350	17.74	141.7	0.39	11.0	9.4	10.6	268.6
Co/RAl_2O_3-450	18.02	141.2	0.37	10.6	9.5	10.8	275.4
Co/RAl_2O_3-550	17.79	126.6	0.26	8.3	10.1	10.4	263.9

[a] The Co contents were measured using ICP-AES. [b] d(Co) = 0.75 d(Co_3O_4), the mean particle size of Co_3O_4 calculated from the XRD diffraction peak at 36.8°. [c] The H_2 desorption amounts and dispersion were calculated from H_2-TPD results.

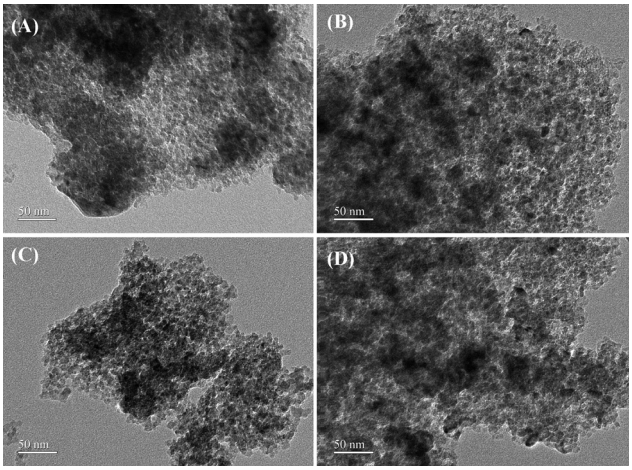

Fig. 3 TEM images of different catalysts: (A) Co/Al_2O_3, (B) Co/RAl_2O_3-350, (C) Co/RAl_2O_3-450, (D) Co/RAl_2O_3-550.

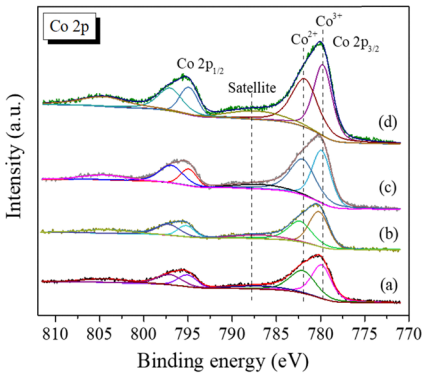

Fig. 4 Co 2p XPS spectra of different catalysts: (a) Co/Al_2O_3, (b) Co/RAl_2O_3-350, (c) Co/RAl_2O_3-450, (d) Co/RAl_2O_3-550.

particular, Co/RAl_2O_3-550 sample possessed the largest amount of available cobalt active sites. Besides, the molar ratios between the peak areas of satellite peak (A_{SS}) and Co^{2+} peak (A_{CSS}) were calculated. Compared with the Co/Al_2O_3 catalyst, the reduced Al_2O_3-supported cobalt catalysts showed high $A_{SS}/(A_{SS} + A_{CSS})$ values, implying the existence of more $CoAl_2O_4$ species.[30,31] The high concentration of $CoAl_2O_4$ species indicated a strong interaction between the cobalt species and the support, which was promoted by the increased defective sites of Al_2O_3 support. Furthermore, a gradual shift was observed toward the low binding energy, from Co/Al_2O_3 to the serial Co/RAl_2O_3-*T* catalysts, indicating that more electrons were transferred from cobalt to Al_2O_3 support. Thus, the reduced Al_2O_3 with defective sites strengthened the MSI. The O 1s XPS results for all the samples are also shown in Fig. S1. Compared with Co/Al_2O_3, the O 1s binding energy in the defective-alumina-supported cobalt catalysts shifted to low binding energy, which indirectly verified the lack of oxygen atoms due to the dehydration and dihydroxylation during the pre-reduction process.

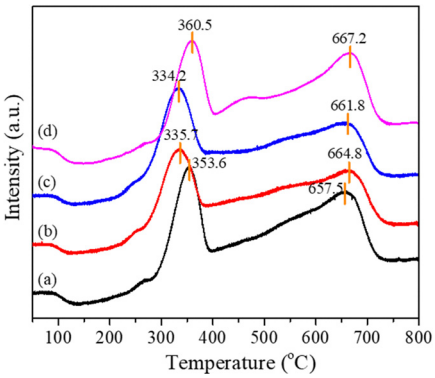

Fig. 5 H_2-TPR profiles of different catalysts: (a) Co/Al_2O_3, (b) Co/RAl_2O_3-350, (c) Co/RAl_2O_3-450, and (d) Co/RAl_2O_3-550.

H_2-TPR analysis was conducted to assess the redox properties of different catalysts. As shown in Fig. 5, two main reduction peaks were clearly observed for all the cobalt catalysts. The one continuous peak between 200 and 500 °C was assigned to the reduction from Co^{3+} to Co^{2+} and Co^0 species.[6,32,33] Compared with Co/Al_2O_3 catalyst, the reduction peaks of Co/RAl_2O_3-350 and Co/RAl_2O_3-450 catalysts shifted to low temperatures except for Co/RAl_2O_3-550, indicating that the moderate reduction of Al_2O_3 support boosted the reduction of cobalt species, which might be linked to the smaller particle size of cobalt oxides, as determined by XRD analyses. The strong reduction of Al_2O_3 support improved the metal–support interaction in Co/RAl_2O_3-550, which delayed the reduction of cobalt oxides. This result agreed well with the XPS finding. As for the reduction peak at a high temperature (*ca.*700 °C), it was associated with the strong reduction of cobalt oxide interacting with alumina or surface $CoAl_2O_4$ species.[34,35] In contrast, Co/RAl_2O_3-550 sample exhibited a reduction peak at the highest temperature, implying the existence of a strong SMI. Besides, H_2-TPR profiles of both the bare and pre-reduced alumina were analyzed (Fig. S3). Clearly, the bare alumina exhibited a weak and continuous reduction in the range of 200–600 °C. For the pre-reduced alumina, the intensity of reduction peak increased significantly, especially for the RAl_2O_3-550 support. This finding indicated that both the reduction of weakly coordinated surface aluminum and strongly coordinated bulk aluminum were improved,[19] which facilitated the interaction between the cobalt species and reduced alumina.

The surface acidity of alumina supported-cobalt catalysts was studied using FTIR spectroscopy, with pyridine as a probe molecule. As shown in Fig. 6, the main adsorbed species of pyridine on the catalyst surfaces were typically featured in the region from 1400 to 1700 cm^{-1}. With an increase in the desorption temperature, the peak intensity of pyridine desorption obviously decreased (Fig. S2), suggesting that the strength of acid sites became weaker. In addition, the bands observed at wavenumbers of *ca.* 1613, 1578, 1542, 1492 and 1450 cm^{-1} were attributed to the 8a, 8b, 19a and 19b ring vibrational modes of molecular pyridine, respectively.[36,37] The bands at *ca.* 1613, 1578, 1492 and 1450 cm^{-1} were ascribed to

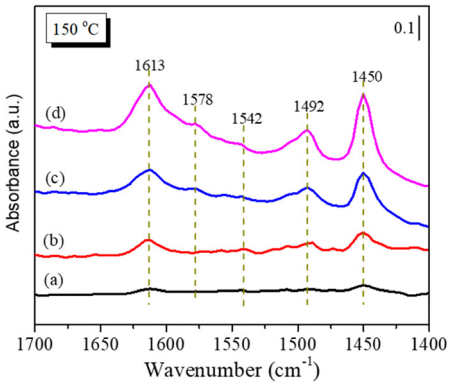

Fig. 6 FT-IR spectra after the adsorption of pyridine followed by desorption at 150 °C of (a) Co/Al_2O_3, (b) Co/RAl_2O_3-350, (c) Co/RAl_2O_3-450, (d) Co/RAl_2O_3-550 catalysts.

the pyridine adsorption on Lewis acid sites, while the band at *ca.* 1542 cm^{-1} was attributed to the pyridine adsorption on Brønsted acid sites.[38,39] Obviously, there existed more L-acid and less B-acid sites over the serial reduced Al_2O_3-supported cobalt catalysts. In contrast, the defective-alumina-supported cobalt (Co/RAl_2O_3-*T*) catalysts possessed a larger amount of L-acid sites than unreduced Co/Al_2O_3. The Co/RAl_2O_3-550 catalyst exhibited the largest amount of L-acid sites.

Fig. 7. A shows the CO-TPD profiles of different catalysts. An obvious CO desorption was exhibited with double peaks at low temperatures (<200 °C). No obvious CO desorption was observed at high temperatures (>500 °C). It was reported that the CO desorption at low and high temperatures could be ascribed to the desorption of CO molecules (CO_{ads}) and the desorption of CO (CO*), originating from the recombination of dissociated C* and O*, respectively.[40–42] Compared with the Co/Al_2O_3 catalyst, the other three defective-Al_2O_3-supported cobalt catalysts showed improved CO desorption behavior. This indicated that defective-alumina-supported cobalt catalysts have more surface-active sites for CO adsorption. According to the FTS reaction mechanism, the CO adsorption on the active sites is the first step, and this CO association is a key step in the reaction pathway.[42] The CO_{ads} species are the important monomeric carbon species in the CO absorption mechanism, while the carbide mechanism correspond to the dissociation of C* and CH_x, and the carbide mechanism was constrained by the adsorption and desorption of the CO molecule.[43] According to the CO-TPD results, it confirms that the serial Co/RAl_2O_3-*T* catalysts have more CO desorption amount compared with the Co/Al_2O_3 catalyst. Meanwhile, we noted that Co/RAl_2O_3-550 catalyst had the lowest CO desorption temperature, whereas the CO desorption peaks of Co/RAl_2O_3-350 and Co/RAl_2O_3-450 catalysts shifted to a higher temperature compared with Co/Al_2O_3. This meant that the lower CO desorption temperature was linked to larger Co particles,[42] showing a relatively weak combination of surface-active species. It might be concluded that more CO desorption and lower desorption temperature contribute to high reactivity. As measured using H_2-TPD (Fig. S4), the corresponding desorbed H_2 amounts and metal dispersion were calculated and are summarized in Table 1. The defective-Al_2O_3-supported cobalt catalysts exhibit a small amount of desorbed H_2 in comparison with Co/Al_2O_3 catalyst, implying a relatively lower Co dispersion. This result is consistent with the XRD and CO-TPD findings, indicating that the Co/RAl_2O_3-550 catalyst has the largest Co particles.

In order to assess the reactivity of surface Co species, CO-TPSR measurements were performed over different catalysts. The formed CH_4 signals were recorded and are depicted in Fig. 7B. Apparently, the signals corresponding to the yield of CH_4 molecules were located at low and high temperature ranges, which originated from the hydrogenation of surface-adsorbed CO_{ads} and dissociated C* species, respectively. We noted that the signals corresponding to the yield of CH_4 for the serial Co/RAl_2O_3-*T* catalysts were more intense than that those for the Co/Al_2O_3 catalyst. Especially, the Co/RAl_2O_3-550 catalyst exhibited the largest CH_4 signal peak, indicating its highest reactivity.

Fig. 8 displays the catalytic performance of different catalysts for the FTS, and the detailed values are listed in Table 2. As shown in Fig. 8, Co/RAl_2O_3-550 catalyst showed the highest activity for CO conversion within 100 h. Co/RAl_2O_3-450, Co/RAl_2O_3-350 and Co/Al_2O_3 showed a similar trend in CO conversion activity, exhibiting a loss of activity with reaction time. In Table 2, the reaction data including product distribution was

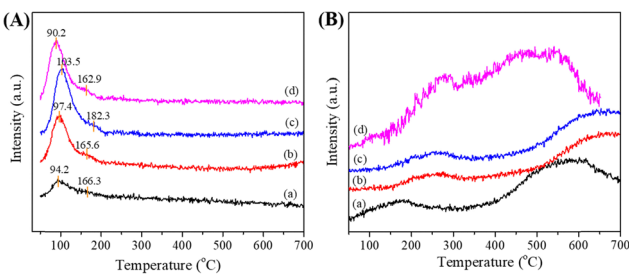

Fig. 7 (A) CO signals of CO-TPD and (B) CH_4 signals of CO-TPSR of different catalysts: (a) Co/Al_2O_3, (b) Co/RAl_2O_3-350, (c) Co/RAl_2O_3-450, and (d) Co/RAl_2O_3-550.

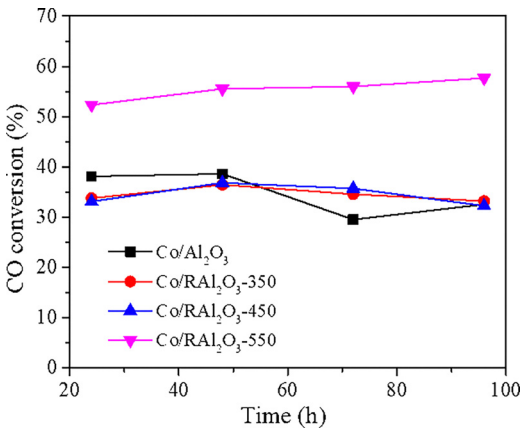

Fig. 8 Catalytic performance of different catalysts. Time-on-stream evolution of CO conversion. Reaction conditions: *T* = 200 °C, *P* = 2 MPa, SV = 1000 h^{-1}, CO/H_2 = 1/2.

Table 2 Catalytic performance of the catalysts

Catalyst	Conv. (CO)[a]/%	CTY (10^{-5}molCO/(g_{Co} s))	TOFs (10^{-3} s^{-1})	$S(CH_4)$/%	$S(C_2–C_4)$/%	$S(C_{5+})$/%
Co/Al_2O_3	29.5	0.8	2.2	6.7	8.7	84.6
Co/RAl_2O_3-350	34.6	0.8	2.6	6.3	8.5	85.2
Co/RAl_2O_3-450	35.7	0.9	3.1	4.4	4.8	90.8
Co/RAl_2O_3-550	56.0	1.1	3.7	2.7	4.1	93.2

[a] The data of the catalytic activity at 72 h were selected. Reaction condition: T = 200 °C, P = 2 MPa, GHSV = 1000 h^{-1}, H_2/CO = 2.

chosen at reaction time of 72 h. Notably, Co/RAl_2O_3-550 catalyst showed the lowest CH_4 selectivity (*ca.* 2.3%) and highest C_{5+} selectivity (*ca.* 93%). In contrast, Co/Al_2O_3 catalyst showed the highest CH_4 selectivity (*ca.* 6.7%) and lowest C_{5+} selectivity (*ca.* 84.6%). This indicated that the pre-reduction of Al_2O_3 support facilitated the improvement of C_{5+} products, while the CO conversion increased sharply when the pre-reduction temperature was increased to 550 °C. These results might be associated with the change in the surface acid property. Because the CO molecules were used as qualitative metrics for the surface Lewis activity,[44] the H_2 reduction of Al_2O_3 support could create more Lewis acid sites based on CO-TPD result. The pyridine adsorption results further confirmed the assumption that the serial defective-alumina-supported cobalt catalysts showed more L-acid sites than Co/Al_2O_3 catalyst. With a rise in the reduction temperature, the amount of L-acid sites increased. The increased Lewis acidity promoted the rate of CO consumption *via* CO dissociation, thereby improving the C_{5+} products and suppressing the yield of CH_4.[45] Besides, the detailed analyses for the products are provided in Table S2, including the selectivity for $C_5–C_{11}$, $C_{12}–C_{18}$, and C_{18+}.

In addition, some representative Co-based catalysts for the FTS are listed in Table S3. Although the previously reported catalysts were evaluated under different reaction conditions, our as-prepared catalysts exhibited good performance, especially in their high selectivity for long-chain paraffins. Based on the above characterizations, it was demonstrated that the Co/RAl_2O_3-550 catalyst exhibited a strong metal–support interaction (SMSI) in comparison with other three catalysts. It can be assumed that the SMSI was helpful for its robust stability.[7] According to H_2 desorption amount measured by H_2-TPD, the surface accessible cobalt atoms were estimated from the H_2 uptake assuming a one to one stoichiometry (H:Co = 1). The corresponding TOFs are summarized in Table 2. Clearly, the Co/RAl_2O_3-550 catalyst showed excellent FTS reactivity (activity per gram of Co (CTY) reached 1.1 × 10^{-5} molCO g_{Co}^{-1} s^{-1} at 200 °C) and TOF (3.72 × 10^{-3} s^{-1}). In brief, the defective-Al_2O_3-supported cobalt catalyst showed superior performance in the FTS.

To further understand the reaction mechanism, *in situ* FTIR spectroscopy was performed on different CO adsorbed-cobalt catalysts (Fig. 9). The intense peaks at 2170 and 2117 cm^{-1} were assigned to gaseous CO adsorption.[46] The band at 2086 cm^{-1} was assigned to surface carbonyl species. In addition, the weak peaks at 2032 and 1934 cm^{-1} corresponded to the linear CO adsorption and bridged CO adsorption, respectively.[47] As seen in Fig. 9A, inset, the Co/Al_2O_3 catalyst possessed the largest amount of linear and bridged CO. For the other three defective-Al_2O_3-supported catalysts, the intensity of linear CO was obviously larger than that of bridged CO. After purging with Ar for 30 min, there was basically no residual gaseous CO (Fig. 9B). Only bridge- and linear-type adsorbed CO were retained on the catalysts. The amount of bridge-type CO outweighed that of the linear type. Fujimoto *et al.*[48,49] proposed that the high density of bridged CO would result in a high probability for chain growth and high C_{5+} hydrocarbon selectivity. Nevertheless, Blekkan *et al.*[50] reported that too strong CO adsorption might make CO dissociation difficult and poison the active sites, with negative effects on the FTS activity and selectivity. Thus, a moderate CO adsorption facilitated a superior performance, regardless of the direct or H-assisted CO dissociation mechanism.

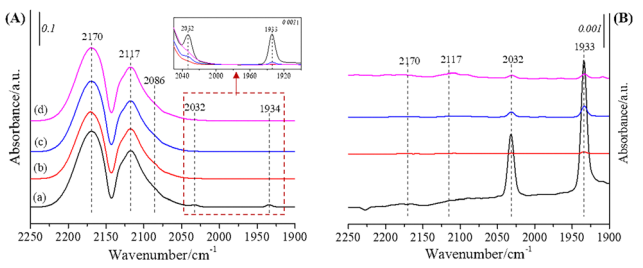

Fig. 9 (A) *In situ* FTIR spectra of different cobalt catalysts at 30 °C, and the enlarged FTIR spectra (inset). (B) FTIR spectra after purging with Ar for 30 min. (a) Co/Al_2O_3, (b) Co/RAl_2O_3-350, (c) Co/RAl_2O_3-450, and (d) Co/RAl_2O_3-550.

Conclusions

In summary, the reduced and unreduced γ-Al_2O_3-supported cobalt catalysts were successfully prepared and applied for the FTS. The reduced Al_2O_3 possessed more defective sites for anchoring the cobalt species. Compared with the Co/Al_2O_3 catalyst, the serial Co/RAl_2O_3-T catalysts showed an improved CO conversion and C_{5+} selectivity and decreased CH_4 selectivity. The Co/RAl_2O_3-550 catalyst displayed a robust FTS stability, which was attributed to the SMSI through the interaction with more defective sites. Besides, the reduction of alumina boosted the number of surface L-acid sites, promoting the CO absorption rate *via* CO dissociation. Studies on the catalyst modification and long-term stability will be carried out in the future. It is expected that this study will provide a practical strategy for the rational design of highly efficient and stable FTS catalysts.

Author contributions

Qiuyao Jiao: methodology, investigation, data curation, writing – original draft. Yan Liu: supervision, resources. Yan Yu: formal analysis, discussion, data curation. Lei Li: supervision. writing – review & editing.

Conflicts of interest

The authors declare that they have no known competing financial interests or personal relationships that could have appeared to influence the work reported in this paper.

Data availability

The data that support the findings of this study are available from the corresponding author upon reasonable request.

Experimental section; O1s XPS spectra of different catalysts; FT-IR spectra after the adsorption of pyridine followed with desorption of Co/Al_2O_3 at different temperatures; H_2-TPR profile of different Al_2O_3 supports; H_2-TPD profile of the Co/Al_2O_3 and Co/RAl_2O_3-*T* catalysts; XPS results of all catalysts; catalytic performance of the catalysts; the FTS performance of the representative Co-based catalysts. See DOI: **https://doi.org/10.1039/d5nj01928a**

Acknowledgements

This work was supported by the Natural Science Foundation of Shanxi Province (No. 202303021221258), the Talent Introduction Project of Yancheng Institute of Technology, and the Postgraduate Research & Practice Innovation Program of Yancheng Institute of Technology (KYCX25 XZ008).

Notes and references

1 A. Y. Khodakov, W. Chu and P. Fongarland, *Chem. Rev.*, 2007, **107**, 1692–1744.
2 S. S. Ail and S. Dasappa, *Renewable Sustainable Energy Rev.*, 2016, **58**, 267–286.
3 J. R. A. Sietsma, J. D. Meeldijk, J. P. Den Breejen, M. Versluijs-Helder, A. J. Van Dillen, P. E. De Jongh and K. P. De Jong, *Angew. Chem., Int. Ed.*, 2007, 46, 4547–4549.
4 P. Munnik, P. E. De Jongh and K. P. De Jong, *J. Am. Chem. Soc.*, 2014, **136**, 7333–7340.
5 P. Munnik, N. A. Krans, P. E. De Jongh and K. P. De Jong, *ACS Catal.*, 2014, **4**, 3219–3226.
6 L. Li, Y. Liu, J. Zhang, M. Xia and W. Ji, *Fuel*, 2022, **329**, 125481.
7 Y. Liu, L. Li, J. Zhang and B. Hou, *Fuel*, 2024, **375**, 132569.
8 X. Sun, A. I. O. Suarez, M. Meijerink, T. Van Deelen, S. Ould-Chikh, J. Zečević, K. P. De Jong, F. Kapteijn and J. Gascon, *Nat. Commun.*, 2017, **8**, 1680.
9 T. W. van Deelen, C. Hernández Mejía and K. P. de Jong, *Nat. Catal.*, 2019, **2**, 955–970.
10 Q. Cheng, Y. Liu, S. Lyu, Y. Tian, Q. Ma and X. Li, *Chin. J. Chem. Eng.*, 2021, **35**, 220–230.
11 C. Qin, B. Hou, J. Wang, G. Wang, Z. Ma, L. Jia and D. Li, *ACS Appl. Mater. Interfaces*, 2019, **11**, 33886–33893.
12 D. Wang, Z. Wang, G. Li, X. Li and B. Hou, *Ind. Eng. Chem. Res.*, 2018, **57**, 12756–12765.
13 C. Liu, Y. He, L. Wei, Y. Zhao, Y. Zhang, F. Zhao, S. Lyu, S. Chen, J. Hong and J. Li, *Ind. Eng. Chem. Res.*, 2019, **58**, 1095–1104.
14 C. Liu, Y. He, L. Wei, Y. Zhang, Y. Zhao, J. Hong, S. Chen, L. Wang and J. Li, *ACS Catal.*, 2018, **8**, 1591–1600.
15 S. Rane, Ø. Borg, E. Rytter and A. Holmen, *Appl. Catal. A Gen.*, 2012, **437–438**, 10–17.
16 S. Rane, O. Borg, J. Yang, E. Rytter and A. Holmen, *Appl. Catal., A*, 2010, **388**, 160–167.
17 Ø. Borg, P. D. C. Dietzel, A. I. Spjelkavik, E. Z. Tveten, J. C. Walmsley, S. Diplas, S. Eri, A. Holmen and E. Rytter, *J. Catal.*, 2008, **259**, 161–164.
18 J. H. Kwak, J. Hu, D. Mei, C. W. Yi, D. H. Kim, C. H. F. Peden, L. F. Allard and J. Szanyi, *Science*, 2009, **325**, 1670–1673.
19 H. Jeong, O. Kwon, B. S. Kim, J. Bae, S. Shin, H. E. Kim, J. Kim and H. Lee, *Nat. Catal.*, 2020, **3**, 368–375.
20 H. Duan, R. You, S. Xu, Z. Li, K. Qian, T. Cao, W. Huang and X. Bao, *Angew. Chem., Int. Ed.*, 2019, **131**, 12171–12176.
21 W. Liu, S. Yang, Q. Zhang, T. He, Y. Luo, J. Tao, D. Wu and H. Peng, *Appl. Catal., B*, 2021, **292**, 120171.
22 K. Murata, T. Shiotani, J. Ohyama, R. Wakabayashi, H. Maruoka, T. Kimura and A. Satsuma, *Catal. Sci. Technol.*, 2021, **11**, 2374–2378.
23 M. Vaarkamp, J. T. Miller, F. S. Modica and D. C. Koningsberger, *J. Catal.*, 1996, **163**, 294–305.
24 P. D. Nellist and S. J. Pennycook, *Science*, 1996, **274**, 413–415.
25 M. Zhu, J. E. Yang, X. Duan, D. Zhang and S. Wang, *Chem. Eng. J.*, 2020, **397**, 125339.
26 P. Ammendola, P. S. Barbato, L. Lisi, G. Ruoppolo and G. Russo, *Surf. Sci.*, 2011, **605**, 1812–1817.
27 Q. Wu, J. Yan, M. Jiang, Q. Dai, J. Wu, M. N. Ha, Q. Ke, X. Wang and W. Zhan, *Appl. Catal., B*, 2021, **286**, 119949.
28 T. Guo, N. Tang, F. Lin, Q. Shang, S. Chen, H. Qi, X. Pan, C. Wu, G. Xu, J. Zhang, D. Xu and Y. Cong, *ChemSusChem*, 2020, **13**, 3115–3121.
29 H. Tian, X. Liu, L. Dong, X. Ren, H. Liu, C. A. H. Price, Y. Li, G. Wang, Q. Yang and J. Liu, *Adv. Sci.*, 2019, **6**, 1900807.
30 S. Guo, C. Niu, Z. Ma, J. Wang, B. Hou, L. Jia and D. Li, *Fuel*, 2021, **289**, 119780.
31 Z. Zsoldos, T. Hoffer and L. Guczi, *J. Phys. Chem.*, 1991, **95**, 798–801.
32 C. Zhang, W. Chu and R. Jiang, *Catal. Lett.*, 2019, **149**, 3058–3065.
33 L. Li, Q. Yang, B. Wang, D. Wang, Y. Peng, J. Li and J. Crittenden, *J. Clean. Prod.*, 2021, **278**, 123920.
34 Z. S. Zhang, X. P. Fu, W. W. Wang, Z. Jin, Q. S. Song and C. J. Jia, *Sci. China: Chem.*, 2018, **61**, 1389–1398.
35 J. K. Han, L. T. Jia, B. Hou, D. B. Li, Y. Liu, Y. C. Liu and R. H. Xuebao, *J. Fuel Chem. Technol.*, 2015, **43**, 846–851.

36 K. A. Layman, M. M. Ivey and J. C. Hemminger, *J. Phys. Chem. B*, 2003, **107**, 8538–8546.
37 T. K. Phung, C. Herrera, M. Á. Larrubia, M. García-Diéguez, E. Finocchio, L. J. Alemany and G. Busca, *Appl. Catal., A*, 2014, **483**, 41–51.
38 P. D. Srinivasan, K. Khivantsev, J. M. M. Tengco, H. Zhu and J. J. Bravo-Suárez, *J. Catal.*, 2019, **373**, 276–296.
39 J. Liu, W. Y. Li, J. Feng and X. Gao, *Mol. Catal*, 2020, **495**, 111148.
40 C. Pauls, D. Przyrembel and K. Christmann, *J. Phys. Chem. B*, 2004, **108**, 14749–14758.
41 R. P. Galhenage, H. Yan, A. S. Ahsen, O. Ozturk and D. A. Chen, *J. Phys. Chem. C*, 2014, **118**, 17773–17786.
42 C. Qiu, B. Wu, S. Meng and Y. Li, *Acta Chim. Sin.*, 2015, **73**, 690–698.
43 J. Schweicher, A. Bundhoo, A. Frennet, N. Kruse, H. Daly and F. C. Meunier, *J. Phys. Chem. C*, 2010, **114**, 2248–2255.
44 H. H. Kung, *Transition Met. Oxides*, 1989, 282.
45 G. R. Johnson and A. T. Bell, *J. Catal.*, 2016, **338**, 250–264.
46 C. Qin, K. Wu, Y. Xu, S. Guo, R. Li, H. Fan, D. Xu and M. Ding, *Cell Reports Phys. Sci.*, 2023, **4**, 101327.
47 Y. Liu, L. Jia, B. Hou, D. Sun and D. Li, *Appl. Catal., A*, 2017, **530**, 30–36.
48 N. Tsubaki, S. Sun and K. Fujimoto, *J. Catal.*, 2001, **199**, 236–246.
49 Y. Zhang, M. Koike, R. Yang, S. Hinchiranan, T. Vitidsant and N. Tsubaki, *Appl. Catal., A*, 2005, **292**, 252–258.
50 N. E. Tsakoumis, E. Patanou, S. Lögdberg, R. E. Johnsen, R. Myrstad, W. van Beek, E. Rytter and E. A. Blekkan, *ACS Catal.*, 2019, **9**, 511–520.

